Two-dimensional modeling of long-term transients in inductively coupled plasmas using moderate computational parallelism. I. Ar pulsed plasmas

Pramod Subramonium[a)]
Department of Chemical Engineering, University of Illinois, 1406 West Green Street, Urbana, Illinois 61801

Mark J. Kushner[b)]
Department of Electrical and Computer Engineering, University of Illinois, 1406 West Green Street, Urbana, Illinois 61801

(Received 30 April 2001; accepted 19 November 2001)

Quantifying transient phenomena such as pulsed operation is important for optimizing plasma materials processing. These long-term phenomena are difficult to resolve in multidimensional plasma equipment models due to the large computational burden. Hybrid models, which sequentially execute modules addressing different phenomena, may not be adequate to resolve the physics of transients due to their inherent iterative nature. In this article, a different modeling approach is described in which a moderately parallel implementation of a two-dimensional plasma equipment model is used to investigate long-term transients. The computational algorithms are validated by comparing the plasma properties for sequential and parallel execution for a steady state case. The physics model is validated by comparison to experiments. Results from the model were used to investigate the transient behavior of pulsed inductively coupled plasmas sustained in Ar. The consequences of varying pulse repetition frequency, duty cycle, power, and pressure on plasma properties are quantified. We found that the electron density, temperature, and source function, and plasma potential, peak beneath the coils during avalanche at the beginning of a pulse, finally attaining a diffusion dominated profile with a small off axis peak. As the pulse repetition frequency decreases, a more pronounced local maximum in plasma potential and electron temperature occurs. [DOI: 10.1116/1.1434964]

I. INTRODUCTION

Low pressure, high plasma density electric discharges, such as inductively coupled plasmas (ICPs), are gaining importance for advanced semiconductor processing for the fabrication of fine features in microelectronics.[1,2] To meet stringent fabrication requirements, different methods of operating these plasma tools are being investigated. For example, ICPs provide the option of decoupling bulk plasma characteristics from the ion energy delivered to the wafer surface, thereby separately controlling the composition of the reactive flux and ion energy. The operating characteristics of these sources can be additionally tailored by modulating the radio frequency (rf) power deposited into the plasma. In this mode of operation, typically referred to as a ''pulsed plasma,'' the rf power to the coil is modulated on–off at frequencies of 10s–100s of kHz. Earlier studies[3–6] have shown that compared to continuous wave (cw) operation pulsed plasmas enable improved control over processing characteristics by selectively modifying the fluxes of reactive species incident on the wafer. Recently, pulsed plasmas have also been used to suppress etching anomalies such as ''notching'' by reducing charge buildup in features.[6]

Hebner and Fleddermann[7] investigated pulse-modulated ICPs in argon and chlorine. Measurements of electron density were performed for peak rf powers between 150 and 400 W at 13.56 MHz, duty cycles between 10% and 70%, and pulse repetition frequencies between 3 and 20 kHz. [Pulse repetition frequency (PRF) refers to the frequency of the square wave modulation of the rf carrier frequency. Duty cycle refers to the fraction of the modulation period that the rf power is applied (see Fig. 1).] They found that during the first 5–30 rf cycles of each pulse, the discharge operated in a capacitive mode with rf variations in the plasma potential and a relatively low electron density. The steady state electron density during the power-on period was observed to be a function of duty cycle and hence average power in chlorine plasmas. This was attributed to the degree of dissociation of Cl_2 (higher with larger duty cycle), thereby producing larger rates of dissociation and less dissociative attachment.

Ashida *et al.*[8] investigated pulsed ICPs in argon at 5 mTorr, 80 W, and a PRF of 10 kHz with a duty cycle of 50%. They found that the electron density was typically higher than that for cw excitation at the same average power. Higher electron densities were obtained at smaller duty cycles as the peak power deposition during the on period is higher. These observations were attributed to higher ionization efficiencies at the leading edges of the power-on pulse, and lower rates of ion diffusion in the off period. Ishigaki *et al.*[9] measured charged particle and neutral radical densities in pulsed ICPs in CF_4/H_2 mixtures at 15 mTorr using Langmuir probes and quadruple mass spectroscopy. Operating conditions were a peak power of 1 kW at 13.56 MHz, duty cycles between 5%

a)Electronic mail: subramon@uiuc.edu
b)Author to whom correspondence should be addressed; electronic mail: mjk@uiuc.edu

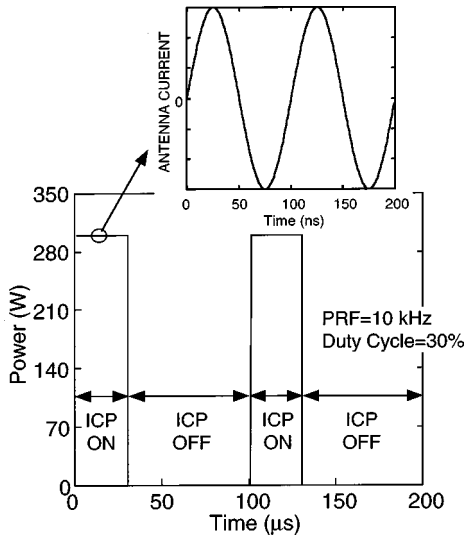

FIG. 1. Time relationships for PRF, power-on period, power-off period, and duty cycle. For the conditions of interest, the power-on and power-off periods are much longer than the electromagnetic rf period.

and 100%, and PRFs between 10 and 100 kHz. They observed that the ratio $CF_x/F(x=2,3)$ increased with lower duty cycle.

Malyshev *et al.*[10] investigated the temporal dynamics of pulsed chlorine ICPs at pressures of 3–20 mTorr with an average power of 500 W, PRF of 10 kHz, and duty cycle of 50%. The electron density during the power-on period reached a peak of 1×10^{10} cm^{-3}. However they observed a large degree of modulation in the electron density during the power-on and power-off cycle as a result of the combined effects of loss of electrons by ambipolar diffusion and dissociative attachment. Malyshev and Donnelly[11] also reported on the dynamics of pulsed chlorine ICPs operated with a continuous rf substrate bias. The conditions were 10 mTorr, average power of 500 W at 13.56 MHz, duty cycle 50%, and PRFs between 0.3 and 10 kHz. The rf bias power was 300 W. They found that there was no significant difference in plasma characteristics with or without the rf bias during the power-on period. When using a rf bias, the electron temperature increased rapidly in the late afterglow of the power-off period after having dropped in the early afterglow. The electron and ion densities decreased in the early off period with or without the bias. The electron density decreased more rapidly in the late afterglow with a rf bias.

Meyyappan[12] investigated pulsed high plasma density Cl_2 and CF_4 discharges using a spatially averaged model. The conditions were 3 mTorr and a peak rf power of 1200 W modulated at 10 kHz with a duty cycle of 25%. Negligible rates of electron impact reactions were predicted during the off part of the cycle. The peak plasma density increased significantly at duty cycles less than 50% for periods of 25–100 μs. In CF_4, the ratio of CF_2/F was only marginally enhanced by pulsing. This finding was attributed to modulation of low threshold electron impact dissociation which simultaneously produces CF_2 and F. Ashida *et al.*[13] Leiberman and Ashida,[14] and Ashida and Leibermann.[15] also investigated pulsed high plasma density, low-pressure plasmas in Ar and Cl_2 using global models. Their conditions were 5 mTorr, time averaged power of 500 W, duty cycle of 25%, and PRF of 1–100 kHz. Their model predicted similar results to those of Meyyappan.[12] For a duty cycle of 25%, the peak plasma density was higher than that with cw at the same average power.

Lymberopoulos *et al.*[16] developed a one-dimensional (1D) fluid model to investigate spatiotemporal dynamics of pulsed ICP Ar plasmas at 10 mTorr. The power was 750 W/m^2 varied at PRFs of 2–100 kHz and duty cycle of 25%. The results showed that generation of superthermal electrons by superelastic relaxation of Ar metastables lengthened the time for the plasma potential to decay in the afterglow. Midha and Economou.[17] computationally studied pulsed chlorine plasmas using a 1D model with base conditions of 20 mTorr, power density of 1 W/cm^3, PRF, of 100 kHz, and duty cycle of 50%. The results showed a separation of the plasma into an ion–ion core and a electron–ion edge during the power-on period of the cycle. A transition from an electron–ion dominated plasma to an ion–ion plasma was observed during the power-off period.

Ramamurthi and Economou[18] investigated pulsed-power Cl_2 ICPs using a 2D fluid simulation. Their results also showed a separation of the plasma into an ion–ion core and an electron–ion periphery. They reported that the evolution of the negative ion density profiles was complex due to the formation of self-sharpening fronts during the plasma-on period and subsequent back-propagation of the fronts during the plasma-off period of the pulse.

In this article, a 2D hybrid model employing moderate computational parallelism is described and results for the spatiotemporal dynamics of electron density, electron temperature, and plasma potential are discussed. The simulations were performed for a Gaseous Electronics Conference Reference Cell (GECRC) modified to include an inductive coil[19] for electropositive argon plasmas. Characteristics of electronegative discharges sustained in Ar/Cl_2 mixtures are discussed in a companion article (Part II).[20] The consequences of varying pulse period, duty cycle, power, and pressure on plasma characteristics were investigated. It was found that the peak electron temperature increased with a decrease in duty cycle. The lower electron density at the end of the longer power-off period resulted in a higher rate of electron heating as a constant power was deposited in a small inventory of electrons. The spatial distribution of the electron temperature had a peak under the coils at the leading edge of the power-on pulse. This peak increased in severity at lower PRFs. The results from the simulation compared well with experiments.

The model is described in Sec. II, followed by a discussion of the validation of the model. The 2D dynamics of pulsed Ar plasmas are discussed in Sec. III. Our concluding remarks are in Sec. IV.

II. DESCRIPTION OF THE MODEL

The model developed for this investigation is a moderately parallel implementation of the Hybrid Plasma Equip-

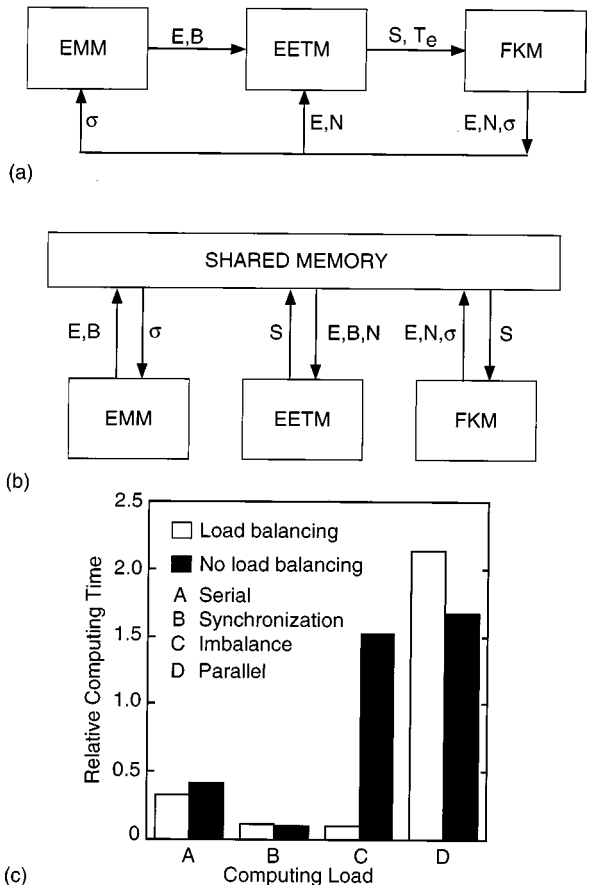

FIG. 2. Schematic of the main body of: (a) the serial HPEM, (b) the HPEM-P, and (c) comparison of computing times. The HPEM sequentially exchange plasma parameters. HPEM-P simultaneously exchanges these parameters through shared memory. Comparison of computing times for various parallel programming operations for a steady state case with and without load balancing are shown as A, B, C, and D. The time spent executing serially is shown as (A), the time spent in synchronization is shown as (B), the imbalance time (the time when processors are idle) is shown as (C) and the time spent in parallel execution is shown as (D). The dynamic load balancing nearly eliminates the time processors are idle.

ment Model (HPEM).[21,22] The HPEM is a modular simulator which iteratively achieves a quasisteady state solution. A flowchart of the HPEM is shown in Fig. 2(a). The main body of the 2D HPEM consists of the Electromagnetics Module (EMM), the Electron Energy Transport Module (EETM), and the Fluid Kinetics Module (FKM). The EMM calculates inductively coupled electric and magnetic fields as well as static magnetic fields produced by the inductive coils, permanent magnets, or dc current coils. The EETM spatially resolves the electron energy transport by either solving the electron energy conservation equation or using the Electron Monte Carlo Simulation (EMCS). The EMCS tracks electron trajectories over many rf cycles to determine spatially dependent electron energy distributions (EEDs). The EEDs are used to generate sources for electron impact processes and electron transport coefficients. Finally, the FKM solves continuity, momentum, and energy equations coupled with Poisson's equation to determine the spatially dependent density of charged and neutral species and electrostatic fields. The modules are iterated to a quasisteady state (average over an rf cycle).

In the computationally serial version of HPEM, the interaction between the modules occurs in the following fashion. The electromagnetic and electrostatic fields produced by the EMM and the FKM are used in the EETM in its next execution (either current or subsequent iteration). EEDs produced in the EETM are used to calculate electron impact source functions for the FKM in its next execution. The spatial distributions of densities produced by the FKM are used to calculate the conductivity for the EMM and collision frequencies in the EETM. These modules are iterated until a converged solution is obtained. Each module receives updates in these quantities at best once each iteration through the model. Although short term transients (e.g., during one rf cycle) are separately captured in each module since the time integration resolves the rf period, the exchange of parameters between modules on longer scales is limited by the ''looping time'' between modules. To properly capture true transients, this looping time must be small compared to the time scale of the transients. In doing so, the expediency of the serial hybrid technique is defeated.

A. Parallel implementation

Since the time scales in plasma simulations are so disparate (e.g., rf dynamics versus gas residence time or plasma decay time), it is our working premise that some type of hybrid scheme is required to model long term transients. To achieve that goal we have developed a parallel implementation of the HPEM, called HPEM-P. In the HPEM-P each of the major modules (EMM, EETM, and FKM) is executed simultaneously on different processors of a moderately parallel computer [see Fig. 2(b)]. In doing so, parameters from the different modules can be exchanged on a frequent and, in some cases, arbitrarily specified basis without interrupting the time evolving calculation being performed in any given module. For example, the plasma conductivity and collision frequency are continuously updated during the execution of the FKM. These updated parameters are made available in shared memory as they are computed so that they can be accessed by the EMM to produce nearly continuous updates of the electromagnetic fields. These more frequent updates of the electromagnetic fields are then made available to the EETM through shared memory, along with parameters from the FKM, updating electron impact source functions and transport coefficients. The electron impact source functions and transport coefficients computed in the EETM are then transferred to the FKM through shared memory, as they are updated, to compute densities, fluxes, and electrostatic fields. Using this methodology, the parameters required by different modules are readily made available ''on the fly'' from other modules.

This method for addressing transients based on moderate parallelism directly interfaces the short plasma time scales with the long-term neutral time scales. Fluid properties (e.g., changes in pressure, mole fractions, and flow fields) which slowly evolve over time are made available to the simulta-

neous calculation of more rapidly changing plasma properties (e.g., electron and ion density, electrostatic fields) through shared memory. The plasma properties will therefore ''track'' (in an almost adiabatic sense) the more slowly varying fluid properties while continually updating electron impact sources.

HPEM-P is codified using a strategy called ''task parallelism.'' In this method, the EMM, EETM, and FKM of the HPEM are executed in parallel as different tasks on three different processors of a symmetric multiprocessor computer having shared memory, as shown in Fig. 2(b). This strategy was implemented using OpenMP compiler directives available for shared memory parallel programming.[23] HPEM-P starts execution as a single thread. The single thread initializes all variables and accesses the required reaction mechanism, fundamental cross section data, and geometrical information for the plasma processing reactor, as was previously done in the serial HPEM. In each iteration of the HPEM-P, the single thread generates three tasks by an explicit spawning technique. Spawning is implemented using PSECTIONS compiler directives, whereby the individual tasks for each processor are explicitly specified by the programmer. In this case, three tasks are to execute the EMM, EETM, and FKM simultaneously by three different threads.

HPEM-P is not a sequentially equivalent version of the HPEM as it allows the individual modules to use the most recent values of plasma parameters available from the other modules. It also does not require a strict order of the access and update of the shared variables. This type of unordered update is often avoided in parallel applications. It is, however, a desirable feature in HPEM-P since the objective is to make the most recent values of plasma parameters from other modules available whenever they are required. Synchronization of the variable updates are, however, needed in order to avoid race conditions from arising due to the continuous updating and accessing of parameters by different modules.

Race conditions arise when unordered memory references to the same location (a read and a write) simultaneously take place from two or more different tasks or modules. When performing parallelization, one first performs a data dependency analysis to establish flow dependence, antidependence, and output dependence in the sequential version of the code. All these dependencies are potentially dangerous with respect to creating race conditions and should be eliminated for the parallel execution to be race free. These dependencies are naturally and frequently encountered in HPEM-P, as variables are updated in shared memory and accessed frequently by the three modules. For example, the FKM may be updating electrostatic fields at the same time they are being read by the EETM. Race conditions are typically eliminated in HPEM-P by the CRITICAL synchronization compiler directive in OpenMP, which defines the scope of a named critical section. The name of the critical section has global scope and two critical directives with the same name are mutually exclusive. This means that if a thread is executing a critical section with a particular name, then any other thread trying to execute the critical section with the same name has to wait until the thread currently executing the critical section exits. Critical sections were defined for the reading and writing of critical and frequently shared variables, such as electron impact source functions, to enable synchronization between the EMM, EETM, and FKM, and so avoid race conditions.

Dynamic load balancing was also required to make the HPEM-P computationally more efficient. Since in the serial HPEM the EMM, EETM, and FKM execute for disparate elapsed times, it is desirable to balance the computational time spent in each module when executing in parallel. This desire is not so much to ensure that processors are not idle but rather to maximize the resolution and accuracy that can be obtained by more frequent updates or using more particles or mesh points. The bottleneck is typically the FKM, which takes the maximum amount of computer time during any given iteration, while the EMM typically takes the least time. A dynamic load balancing strategy was employed to equalize the computer time for each task. First, the computer time spent in the EMCS of the EETM was dynamically adjusted between iterations to make the execution time of the EETM nearly the same as the FKM. If the FKM requires more time to execute than the EETM, then the time in the EMCS is reduced, and vice versa. This is typically accomplished by adding or removing pseudoparticles or by adjusting the number of rf cycles over which the EEDs are computed. By tracking which processor (that is, which module) completes its task first in the current iteration, the time in the EMCS for the next iteration is correspondingly modified. The imbalance between the EETM and the FKM was, to a large extent, successfully reduced by this methodology.

There is, however, a minimum amount of time that must be spent in the EMCS to generate acceptable statistics and so there is a limit to one's ability to load balance. For example, in the event that the FKM is the more rapidly executing module due to the need to acquire acceptable statistics in the EMCS, one can improve the resolution of FKM by, for example, making the mesh finer without any additional computational cost. Since the FKM is executed on a numerical mesh, its execution time scales with its resolution. The EMCS, being a particle simulation, is less sensitive to mesh resolution.

The execution times in the EETM and the EMM were made nearly equal by executing the EMM repeatedly during an iteration when conductivities or powers were changed or updated significantly. Since the fields are strictly used only in the EETM, the EMM is repeatedly executed only until the EETM is completed in each iteration.

The execution times with and without dynamic load balancing are shown in Fig. 2(c) for a typical case to be discussed later. With dynamic balancing, the computational load on the processor executing the EMM and the EETM was increased to match the load on the processor executing the FKM. Thus all three processors executed for nearly the same length of time.

B. Algorithms and options

For the cases discussed in this article, the following options were employed using algorithms in the cited references.

1. EMM

Maxwell's equations were solved in the frequency domain using the method of successive over relaxation.[21]

2. EETM

Electron energy distributions were obtained using a Monte Carlo simulation.[21] Electromagnetic fields from the EMM (amplitudes and phases) and electrostatic fields (binned according to phase in the rf cycle) as a fraction of position are interpolated to obtain accelerations to advance particle trajectories. Collisions are handled using Monte Carlo techniques with gas densities obtained from the FKM.

3. FKM

Continuity, momentum, and energy equations are individually integrated for each neutral and ion species. Momentum transfer and energy coupling terms are included between each species.[22] A drift–diffusion formulation is used for electrons to enable a semi-implicit solution of Poisson's equation for electric potential.[22]

The physics and transport algorithms used in HPEM-P are fundamentally the same as previously described with the exception of the solution of Poisson's equation. The method used here is a semi-implicit solution in which future values of electrostatic potential Φ for time $t+\Delta t$ are predicted based on changes in charge density ρ resulting from divergences in charged particle fluxes φ,

$$-\nabla\cdot\varepsilon\nabla\Phi(t+\Delta t)=\rho(t)+\frac{d\rho(t)}{dt}\cdot\Delta t$$

$$=\rho(t)t+\sum_i q_i\Delta t[(-\nabla\cdot\vec{\varphi}_i)+S_i], \quad (1)$$

where ε is the permittivity, and the sum is over charged particles. S_i are flux independent sources. The implicitness in Φ results from the dependence of fluxes φ_i on the potential. When solving the ion momentum equations φ_i for the ions is held constant in the solution of Eq. (1) and so the implicitness rests in the dependence of electron flux φ_e on the potential.

In previous works, we set

$$\vec{\varphi}_e=-D_e\nabla n_e+qn_e\mu_e\nabla\Phi, \quad (2)$$

where D_e and μ_e are the electron diffusion coefficient and mobility for electron density n_e. In this work, we instead used the Scharfetter–Gummel discretization for fluxes.[24] In this method the flux $\varphi_{i+(1/2)}$ between density mesh points $(i,i+1)$ separated by Δx is given by

$$\varphi_{i+(1/2)}=\frac{\alpha\bar{D}(n_{i+1}-n_i\exp(\alpha\Delta x))}{(1-\exp(\alpha\Delta x))}, \quad (3)$$

where

$$\alpha=-q\bar{\mu}\left(\frac{\Phi_{i+1}-\Phi_i}{\Delta x}\right)$$

and $\bar{D}$ and $\bar{\mu}$ are the average diffusion coefficient and mobility in the interval. The form of Eq. (1) solved is then

$$-\nabla\cdot\varepsilon\nabla\Phi=\rho_0+\sum_i q_i\Delta t[(-\nabla\cdot\vec{\varphi}_{i0})+S_{i0}]+q_e\Delta t\Bigg(-\nabla\cdot\left(\vec{\varphi}_{e0}+\frac{\partial}{\partial\Phi}(\vec{\varphi}_{e0})(\Phi-\Phi_0)\right)+S_{e0}\Bigg), \quad (4)$$

where the subscript 0 denotes quantities evaluated at t and those quantities without such subscripts are evaluated at $(t+\Delta t)$. The Jacobian element $(\partial/\partial\Phi)(\vec{\varphi}_{e0})$ is numerically evaluated by perturbing Φ by a small fractional value and computing the change in $\vec{\varphi}_e$. Equation (4) is solved for Φ using the method of successive over-relaxation.

C. Computational validation of HPEM-P

The HPEM-P is not a 1-to-1 numerically equivalent implementation of the serial HPEM. However, it should be a physically equivalent implementation. HPEM-P was therefore validated by comparing the sequential and parallel results for a steady state simulation to ensure that the representation of physics had not been detrimentally affected. To validate the HPEM-P numerics, an inductively coupled GECRC[19] was modeled, a schematic of which appears in Fig. 3(a). The conditions were Ar at 20 mTorr, 300 W, and a flow rate of 20 sccm. Electron densities for serial and parallel computations in the steady state are shown in Figs. 3(b) and 3(c). The spatial distributions and magnitude are essentially the same peaking at about 8×10^{11} cm^{-3}, although HPEM-P produces a higher electron density by 3%–5%. The temporal evolution of electron temperature T_e, for the serial and parallel cases is shown in Fig. 4. Although in the steady state, T_e is subject to Monte Carlo produced noise, the long term values of the serial and parallel versions are essentially the same. At startup, the HPEM-P better captures the high T_e required for avalanche from the initially low electron density to the steady state.

D. Performance evaluation

Although decreasing the computing time is not the primary concern of this investigation, the improvement in computer performance obtained with HPEM-P is promising. A nearly linear speedup of 2.8 can be achieved on a three processor SUN Microsystems E450 server with SuperSparc II processors. At best, the time required by the HPEM-P can be reduced to the time required by the most CPU intensive module, which in these simulations is the FKM module. In HPEM-P, load balancing enables one to increase the problem size and execute in less time.

III. ARGON PULSED PLASMAS

In this section, the results from our investigation of pulsed argon ICPs in the GECRC are presented. The consequences

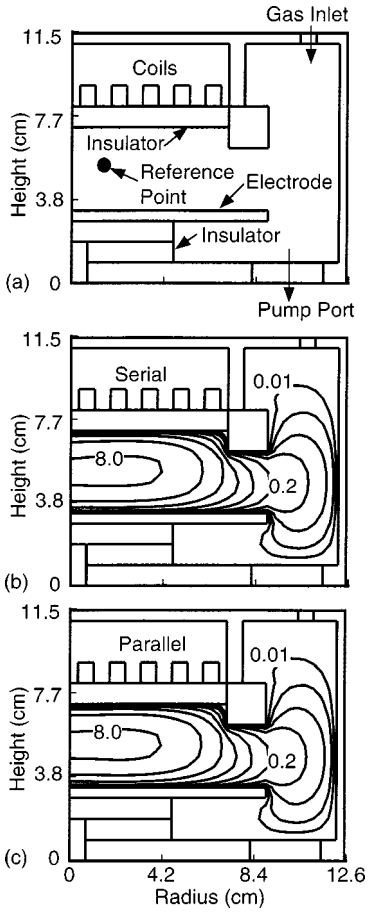

FIG. 3. Comparison of electron densities for serial and parallel cases for steady state conditions in an argon plasma with a power of 300 W and gas flow rate of 20 sccm: (a) schematic of the GECRC, (b) computationally serial derived electron density, and (c) computationally parallel derived electron density. Contours are labeled in units of 10^{11} cm^{-3}. The parallel and serial implementations produced the same profiles of electron density within 3%–5%.

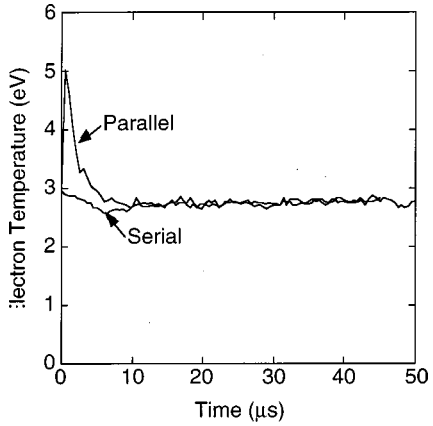

FIG. 4. Comparison of electron temperature for a serial and parallel cases for steady state conditions with a power of 300 W, pressure of 20 mTorr of argon, and gas flow rate of 20 sccm. The parallel case better captures the high temperature startup transient.

of duty cycle, power, pulse repetition frequency, and pressure on plasma properties will be discussed. The simulations were performed by specifying a duty cycle, PRF, and peak rf power during the on cycle. A time averaged power is then computed and the HPEM-P is executed on a cw basis using this power to establish a steady state in electron and ion density, gas temperature, and gas flow field. Acceleration techniques are used during this baseline phase to speed the numerical convergence. When using acceleration it is difficult to correlate the elapsed integration time with the real elapsed physical time. Once this baseline is established the acceleration is therefore turned off and the power is pulsed at the specified PRF and duty cycle. The ramp up to the peak power in the power-on state and ramp down to the power-off state are 5 and 17 μs, respectively. Successive pulses are computed until a pulse periodic steady state is achieved, which typically requires 4–10 pulses. The power was reduced to 3×10^{-3} W during the ramp down and kept at this value for the power-off period. The off power is not set to zero due to numerical issues which require a nonzero power. The off-period power is sufficiently low that no significant electron heating occurs.

To validate the physics model, the results of the simulation were compared to experiments by Hebner and Fledderman[7] who characterized pulse modulated ICPs in argon sustained in a GECRC. The time dependent electron column density was measured using microwave interferometry as a function of duty cycle, PRF, and power. An equivalent electron column density was obtained from the model by radially integrating the electron density at a height of 2 cm above the substrate. The Ar reaction chemistry is given in Table I. Computed and experimental results for a peak power of 300 W, PRF of 10 kHz, and duty cycle of 50% at 20 mTorr are shown in Fig. 5. Comparisons are shown for a

TABLE I. Ar reaction mechanism.[a]

Reaction	Rate coefficient (cm^{-3} s^{-1})	Reference
$e+\mathrm{Ar}\rightarrow\mathrm{Ar}^*+e$	b	26
$e+\mathrm{Ar}\rightarrow\mathrm{Ar}^{**}+e$	b	26
$e+\mathrm{Ar}\rightarrow\mathrm{Ar}^+ +e+e$	b	27
$e+\mathrm{Ar}^*\rightarrow\mathrm{Ar}^+ +e+e$	b	28
$e+\mathrm{Ar}^*\rightarrow\mathrm{Ar}+e$	b	d
$e+\mathrm{Ar}^*\rightarrow\mathrm{Ar}^{**}+e$	b	29
$e+\mathrm{Ar}^{**}\rightarrow\mathrm{Ar}+e$	b	d
$e+\mathrm{Ar}^{**}\rightarrow\mathrm{Ar}^+ +e+e$	b	30
$e+\mathrm{Ar}^{**}\rightarrow\mathrm{Ar}^*+e$	b	d
$\mathrm{Ar}^*+\mathrm{Ar}^*\rightarrow\mathrm{Ar}^+ +\mathrm{Ar}+e$	5×10^{-10}	c
$\mathrm{Ar}^{**}+\mathrm{Ar}^{**}\rightarrow\mathrm{Ar}^+ +\mathrm{Ar}+e$	5×10^{-10}	b
$\mathrm{Ar}^{**}+\mathrm{Ar}^*\rightarrow\mathrm{Ar}^+ +\mathrm{Ar}+e$	5×10^{-10}	b
$\mathrm{Ar}^{**}\rightarrow\mathrm{Ar}^*$	1×10^{6}	e

[a]Only reactions which change the density of a species are shown. All pertinent electron impact processes, such as elastic collisions, are included in the EMCS. Ar* is nominally the Ar($4s$) manifold. Ar** is nominally the Ar($4p$) manifold.
[b]Rate coefficients are calculated from electron energy distribution obtained in the EMCS.
[c]Estimated.
[d]Cross section obtained by detailed balance.
[e]See text.

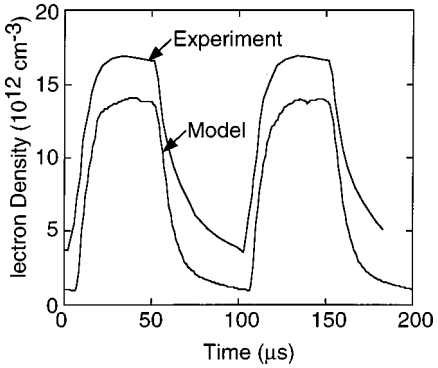

FIG. 5. Comparison of experimentally measured electron column density with results from the model for a peak power of 300 W, PRF of 10 kHz, and duty cycle of 50% in argon.

physics model in which the Ar($4s$) manifold is represented by a lumped metastable state, reflecting a high degree of radiation trapping.[25] The Ar($4p$) manifold has an effective lifetime of 1 μs, also reflecting some degree of radiation trapping. The experimental and computed results are in good agreement, and within experimental uncertainty.

Parameterizations were performed for pulsed ICPs in argon in the GECRC. The base case conditions were 20 mTorr with a peak power of 300 W modulated at a PRF of 10 kHz and a duty cycle of 50%. The duty cycle was varied from 10% to 70% and the pulse repetition frequency was varied from 5 to 20 kHz. The peak power was varied from 165 to 300 W, while the pressure was varied from 10 to 30 mTorr.

The electron density and electron temperature for the base case are shown in Fig. 6. These values are for the reference location noted in Fig. 3(a). When the plasma is turned off, the electron density decays monotonically. The time scales of electron decay are determined by the ambipolar loss of ions to the walls. For an average electron temperature of 1 eV during the early afterglow, the rate of ambipolar loss for argon ions is approximately 6.5×10^4 s^{-1} or a decay time of approximately 16 μs. [This rate was obtained using a standard temperature and pressure mobility for Ar^+ of 1.53 cm^2/(V s) and transverse diffusion boundaries of 4 cm.] This rate of loss agrees well with the rate of electron and ion loss obtained from the model. As the electrons cool in the latter part of the afterglow the rate of ambipolar losses also decreases. For example, just prior to ramping up the power, the electron temperature is approximately 0.15 eV. This temperature produces an ambipolar decay time of approximately 80 μs, which again agrees with the rate obtained from the model.

The steady state electron temperature is about 2.8 eV. By solving Boltzmann's equation for the electron energy distribution, one finds that for these conditions that the electron energy decay time is less than 1 μs, which is shorter than the power ramp-down time of 17 μs. The fall in T_e at the beginning of afterglow is therefore determined by the ramp down in power deposition. The Ar($4s$) density at the beginning of the afterglow is 2.3×10^{12} cm^{-3}, resulting in the majority of the electron cooling being by inelastic excitation out of the

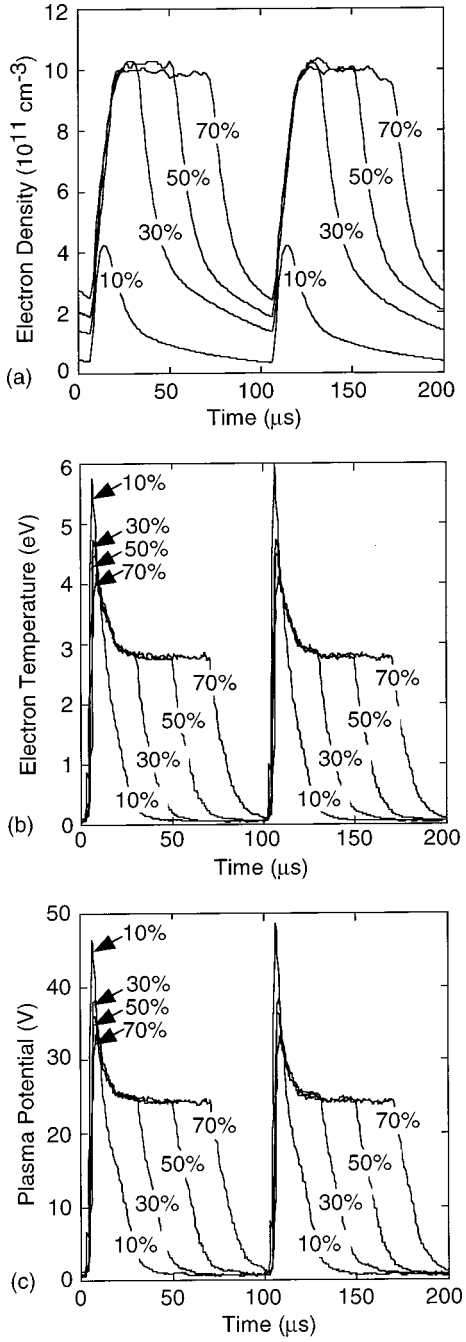

FIG. 6. Plasma properties in argon as a function of time for different duty cycles for a constant peak power of 300 W, PRF of 10 kHz, and gas flow of 20 sccm: (a) electron density at the reference point, (b) electron temperature, and (c) plasma potential. Steady state electron densities are obtained for duty cycles $\geqslant$30%. The electron temperature peaks at lower duty cycle due to the lower electron density at the end of the afterglow.

Ar($4s$) state to Ar($4p$) and by ionization to Ar^+. There is also a component of electron heating by superelastic relaxation of Ar($4s$), as noted by Lymberopoulos *et al.*[16] As the electrons cool during the afterglow and the Ar($4s$) density decreases, the rate of power loss by collisions also decreases, resulting in a slowing of the decay in electron temperature. For example, approximately 15 μs into the afterglow, the electron temperature has decreased to 1 eV, the Ar($4s$) den-

sity has decreased to 1.9×10^{12} cm^{-3}, and the electron relaxation time has increased to approximately 6 μs. Halfway through the afterglow, T_e is about 0.2 eV with an energy relaxation time of 15 μs.

During the power-on period the electron density reaches a steady value nearly equal to that for cw operation in about 25 μs. The increase in electron temperature at the leading edge of the power-on pulse is commensurate with the 5 μs ramp-up time in power deposition, a consequence of the rapid response time of electrons to the higher rate of heating. The peak in T_e at the leading edge of the power-on pulse above that of the steady state value is required to avalanche the plasma to a higher density. Equivalently, a fixed amount of power dissipated by a smaller inventory of electrons produces a higher temperature. For example, at the beginning of the power-on period, the volume integrated electron population is about 1.5×10^{14}, requiring a power deposition of 22 MeV/s to account for 300 W. This corresponds (on a volume averaged basis) to an electron temperature of about 4.2 eV [where the Ar($4s$) mole fraction is 5×10^{-4}] well above the steady state temperature of about 2.8 eV.

The duty cycle was varied from 10% to 70% at a PRF of 10 kHz, peak power of 300 W, and pressure of 20 mTorr. The electron densities at the reference point are shown in Fig. 6(a) for duty cycles of 10%, 30%, 50%, and 70%. The electron temperatures are shown in Fig. 6(b). The avalanche time required to achieve the steady state electron density of 1×10^{12} cm^{-3} is about 25 μs. The electron density therefore has time to reach a steady state value for duty cycles of 30%, 50%, and 70%, but has insufficient time to do so for a duty cycle of 10%, reaching a density of only 4.4×10^{11} cm^{-3}. In a similar fashion, the electron temperature for duty cycles $>30\%$ reaches the steady state value of 2.8 eV during the power-on period. At shorter duty cycles, the electron temperature is, on average, higher than the steady state value during the on period, thereby potentially having higher excitation efficiencies. At shorter duty cycles, the interpulse period is long enough that the electron temperature essentially thermalizes during the afterglow. As a result, the rate of ambipolar diffusion is low and the plasma decay time is longer. Larger duty cycles result in higher time averaged plasma densities and lower electron temperatures during the power-on period.

The plasma potential Φ_p roughly scales with the electron temperature. Φ_p at the leading edge of the power-on period is about 45 V for a duty cycle of 10%, while Φ_p is about 33 V for a duty cycle of 70% [see Fig. 6c)]. For duty cycles greater than 30%, Φ_p attains a steady state value of approximately 25 V. In the off period Φ_p decreases to a few volts in about 20 μs.

Electron densities at different times during a modulation cycle are shown in Fig. 7 for a 50% duty cycle. The ionization source functions by electron impact for the same conditions are shown in Fig. 8. When the power is turned on, the electron source peaks beneath the coils. During the avalanche stage, the electron source is large relative to the rate of loss and so the electron density also peaks under the coils.

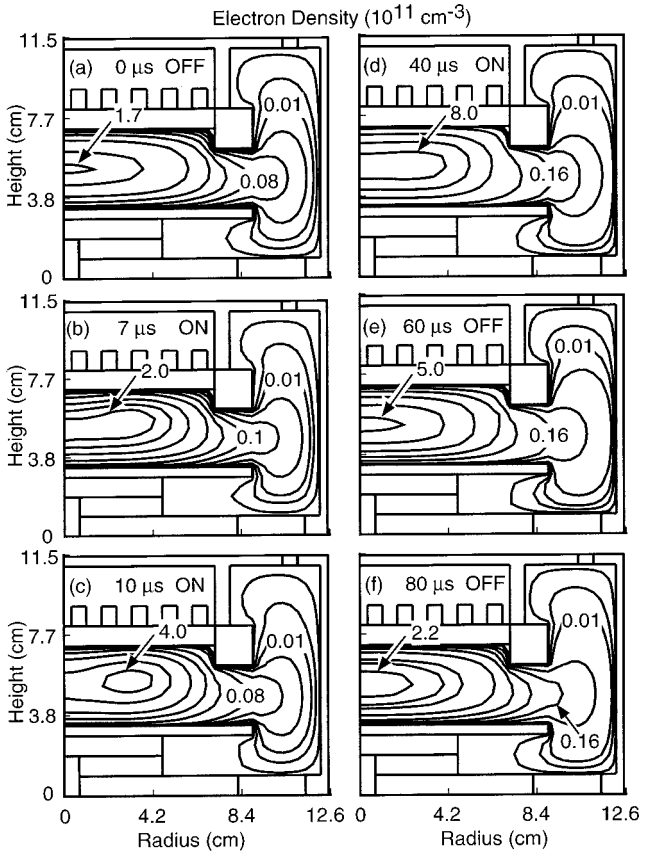

FIG. 7. Electron density in argon plasmas at different times for a power of 300 W, PRF of 10 kHz, and duty cycle of 50%. The power is turned off at 50 μs. Results are shown for: (a) 0 μs, (b) 7 μs, (c) 10 μs, and (d) 40 μs during the power-on period and (e) 60 μs and (f) 80 μs during the afterglow. Contours are labeled in units of 10^{11} cm^{-3}. The electron density is more non uniform during the initial avalanche.

As time progresses, the electron source under the coil decreases as the electron temperature falls to its steady state value. The electron profile correspondingly becomes diffusion dominated, as shown in Fig. 7(d), with a small off axis peak. In the early afterglow, just after the power is turned off at 60 μs, the ambipolar losses dominate over the generation of electrons, resulting in a rapid decrease in the electron density as seen in Fig. 7(d). Since the ambipolar losses scale with the electron temperature, and T_e decreases to a few tenths of an eV as the afterglow progresses, the rates of electron decay also slow in the late afterglow. The decay in electron density is at first most rapid in the center of the plasma where diffusion lengths are shorter, electron temperatures are higher, and rates of ambipolar losses are greater. The spatiotemporal dynamics of electron density for the other duty cycles are similar to the 50% duty cycle case. At lower duty cycles, the power is off for a longer time, resulting in a lower electron density near the walls in the late afterglow.

For the powers and pressures investigated, the steady state electron density scales nearly linearly with power. For example, the peak power was varied from 165 to 300 W. For 300 W at 30% duty cycle, the peak electron density n_e was 1×10^{12} cm^{-3}, while for 190 W, n_e was about 7

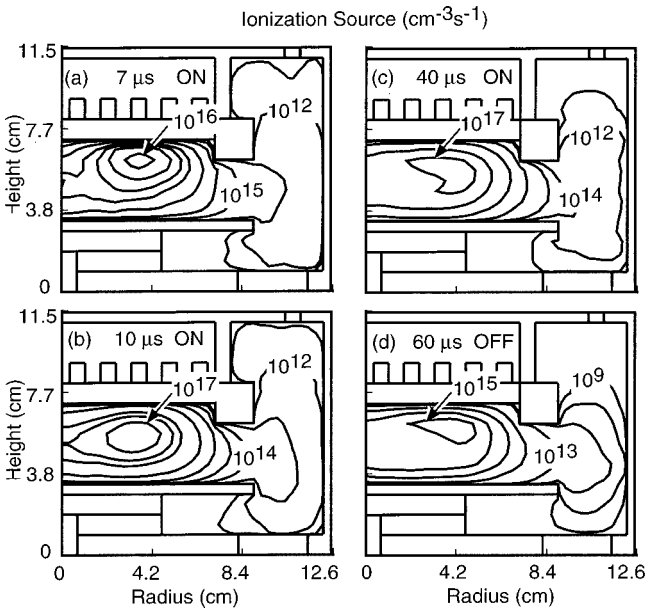

FIG. 8. Electron source function in an argon plasma at different times for a PRF of 10 kHz and duty cycle of 50%. The power is turned off at 50 μs. Results are shown for: (a) 7 μs, (b) 10 μs, and (c) 40 μs during the power-on period, and (d) 60 μs during the afterglow. The electron source is maximum under the coil during the initial avalanche.

$\times 10^{11}$ cm^{-3}. However, for small duty cycles, where the electron density does not attain a steady state the linear relationship between power and electron density does not necessarily hold. For a given duty cycle, T_e is at best a weak function of power. When the power is turned off, the electron density decreases with similar decay times for different powers. This is because the electron density decay rates depend on the rate of ambipolar ion losses, which in turn depends on the ion mobility and electron temperature, neither of which change significantly with power deposition. The spatiotemporal dynamics in electron density were in fact found to be similar for powers of 165, 190, and 300 W with the exception of magnitude.

The electron density, electron temperature, and plasma potential at the reference point shown in Fig. 3(a) for PRFs of 5, 10, and 20 kHz and a 50% duty cycle are shown in Fig. 9. The electron densities in the late afterglow just prior to turning on the power and in the late active glow just prior to turning off the power are shown in Fig. 10. For a fixed duty cycle, higher PRFs produce shorter on and off periods. In the case of 20 kHz and 50% duty cycle, the power-on period is barely sufficient to achieve the steady state electron density of 1×10^{12} cm^{-3}. The electron temperature and plasma potential similarly just achieve their steady state values for 20 kHz. Lower PRFs, having longer afterglow periods, allow the electron density to decay to a lower value, however the decay dynamics are essentially the same regardless of frequency due to T_e and Φ_p being the same at the start of the afterglow.

The time averaged electron density generally increases as the PRF increases due to the shorter interpulse period. The time averaged electron temperature and plasma potential also

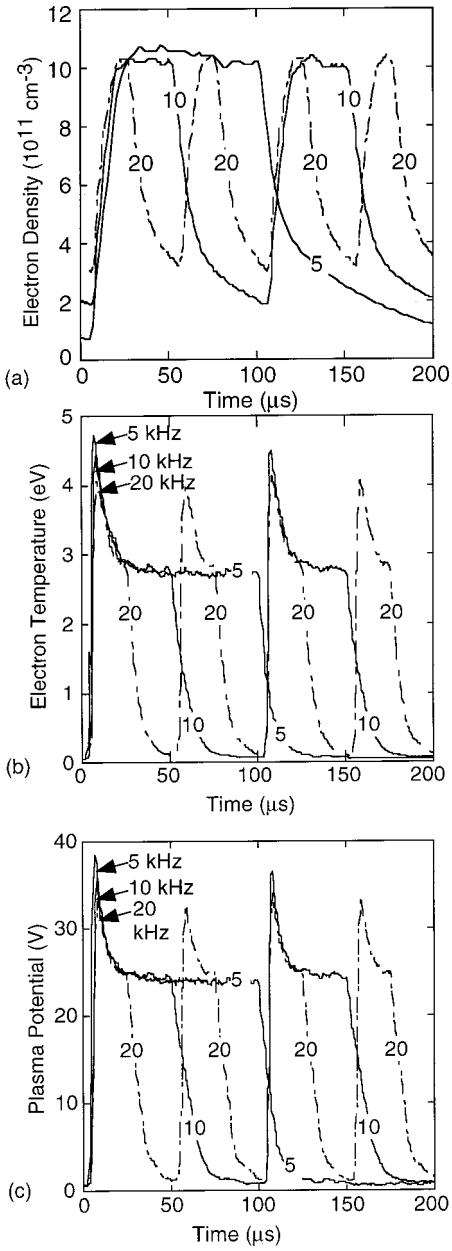

FIG. 9. Plasma properties in argon as a function of time for different PRFs for a constant peak power of 300 W, duty cycle of 50%, and gas flow of 20 sccm: (a) electron density at the reference point, (b) electron temperature and (c) plasma potential. Low PRFs with longer afterglows produce higher leading edge T_e and potential.

increase with increasing PRF as the startup transient occupies a larger fraction of the cycle. The spatial variations in electron density are not strong functions of frequency, as shown in Fig. 10. Since all frequencies achieve the steady state electron density during the power-on time, the spatial distributions are similar in the late active glow. In the late afterglow, we see differences in these spatial distributions. The distributions for high PRF are most similar to those in the active glow due to the shorter interpulse period. The distributions for low frequency, having a longer interpulse period, are more depleted in the periphery of the reactor.

The spatial variations of plasma potential and electron

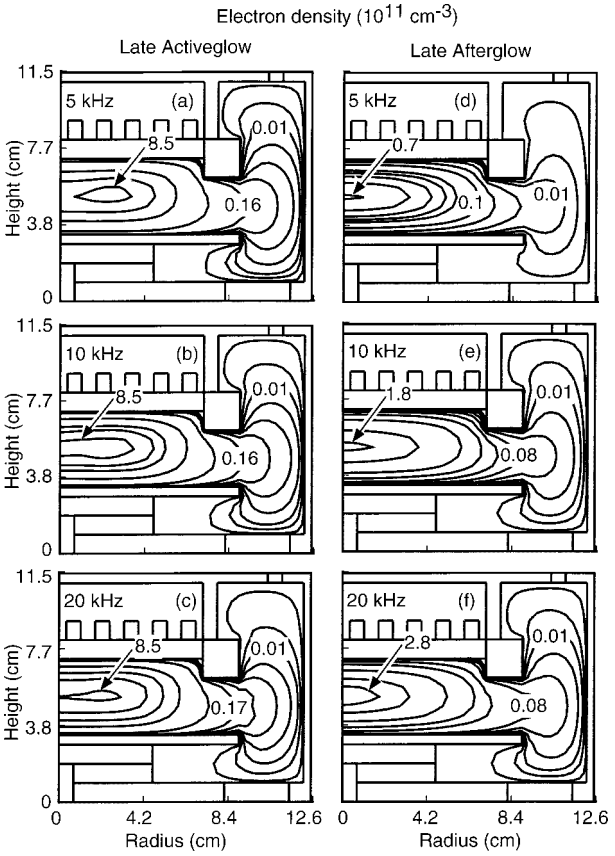

FIG. 10. Electron density in argon plasmas in the late afterglow and late active glow as a function of PRF for a peak input power of 300 W and duty cycle of 50%. Results shown are at the end of active glow for: (a) 5 kHz, (b) 10 kHz, and (c) 20 kHz and at the end of afterglow for (d) 5 kHz, (e) 10 kHz, and (f) 20 kHz. Contours are labeled in units of 10^{11} cm^{-3}.

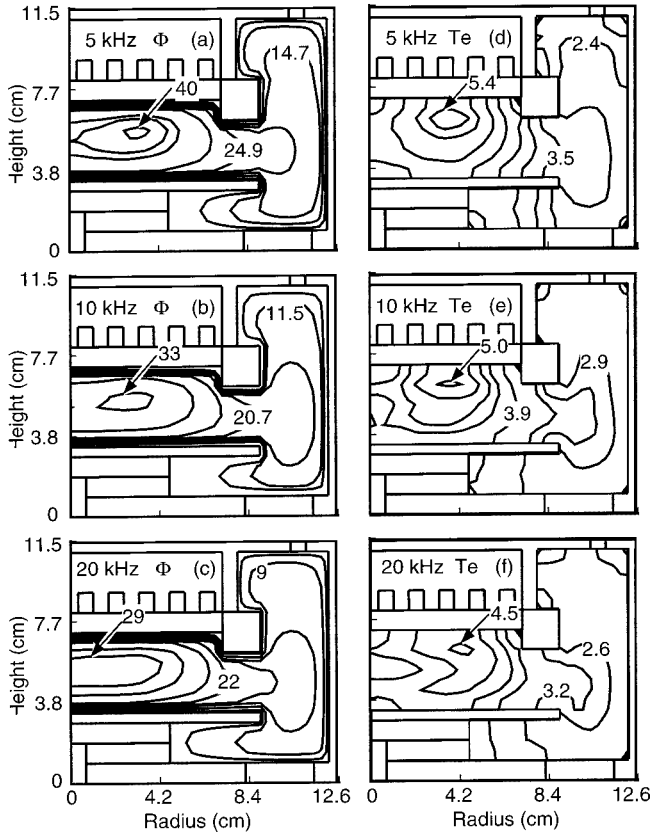

FIG. 11. Plasma potential (Φ, V) and electron temperature (T_e, eV) when the peak in electron temperature occurs during the leading edge of the power-on pulse as a function of PRF for a peak input power of 300 W and duty cycle of 50%.

temperature with pulse repetition frequency are shown in Fig. 11 for the leading edge of the power-on portion of the pulse. The peak plasma potential [see also Fig. 9(c)] was highest for the lowest pulse repetition frequency (40 V for 5 kHz) and decreased with the increase in the frequency (29 V for 20 kHz). The peak electron temperature was 5.4 eV for 5 kHz and 4.5 eV for 20 kHz. The decay times for the plasma potential and T_e were ≈ 20 μs for all the frequencies as they are largely a function of collision frequency, which depends on pressure. Φ_p and T_e are higher for the lower pulse repetition frequencies because the electron density is initially lower due to the longer interpulse period. Higher electron temperatures are needed to avalanche the plasma from the lower electron density and a higher electron temperature is required for the smaller inventory of electrons to dissipate the desired power. It should be noted that as the PRF decreases the local maximum in Φ_p and T_e beneath the coils becomes more pronounced. This is due to the shorter energy relaxation distance at the higher electron temperature, which localizes the electron temperature (and hence plasma potential) to where the electric field and electron acceleration are largest.

Pressure has a significant effect on the spatiotemporal dynamics of plasma properties. For example the time evolution of electron density at the reference point, electron temperature and plasma potential are shown in Fig. 12 for 10 and 30 mTorr. The electron densities in the late active glow and late afterglow for 10 and 30 mTorr are shown in Fig. 13. The peak power is 300 W, PRF is 10 kHz, and duty cycle is 30%. The electron density is marginally higher at 30 mTorr, a reflection of the lower rate of diffusion losses. The peak electron temperature at 10 mTorr is correspondingly higher, a consequence of the need for larger ionization rates to balance the larger diffusion losses. The lower collision frequency at 10 mTorr also requires a higher T_e to dissipate 300 W for approximately the same electron density. The plasma potential shows a similar behavior. The peak plasma potential was 48 V at 10 mTorr, while it was 31 V at 30 mTorr. The peak electron density in the late afterglow is higher and more confined at 30 mTorr as the rates of diffusion losses are lower at higher pressures. The electron density is more diffused and lower in the late afterglow at the lower pressure. The electron temperature peaks at 5.8 eV at the leading edge of the power-on pulse at 10 mTorr, while peaking at 3.9 eV at 30 mTorr. The electron density in the late afterglow is lower at lower pressures due to the higher rate of diffusion loss.

IV. CONCLUDING REMARKS

A two-dimensional hybrid model based on moderate computational parallelism was developed for addressing tran-

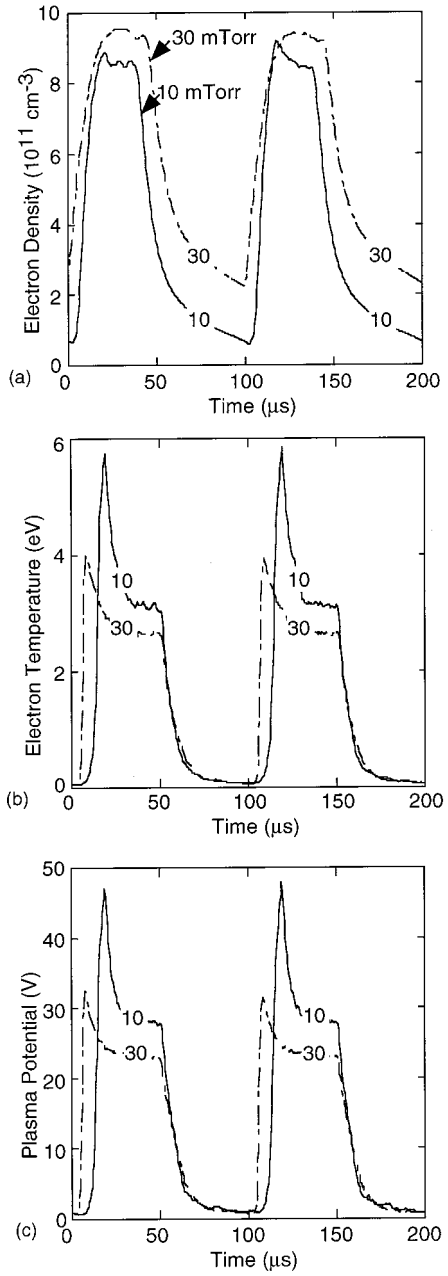

FIG. 12. Plasma properties in argon as a function of time for 30 and 10 mTorr for a constant peak power of 300 W, PRF of 10 kHz, duty cycle of 30%, and gas flow of 20 sccm: (a) electron density at the reference point in Figs. 3(a), (b) electron temperature, and (c) plasma potential.

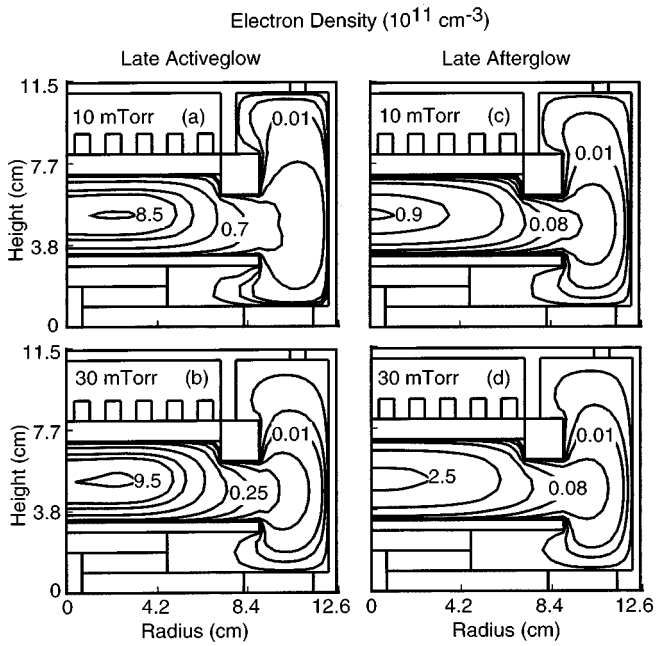

FIG. 13. Electron density in an argon plasma in the late afterglow (a)–(b) and late active glow (c)–(d) as a function of pressure for a peak power of 300 W, PRF of 10 kHz, and duty cycle of 50%. Results shown are at the end of the active glow for: (a) 10 mTorr and (b) 30 mTorr and at the end of the afterglow for (c) 10 mTorr and (d) 30 mTorr. Contours are labeled in units of 10^{11} cm^{-3}.

sients in low pressure plasmas. This method interfaces the short plasma time scales with the long-term neutral time scales. Fluid conditions (e.g., changes in pressure, mole fractions, and flow fields) which are slowly evolving over time are made available to the simultaneous calculation of plasma properties (e.g., electron and ion density, electrostatic fields) through shared memory. Functionally, short time scale phenomena track the long scale phenomena in an adiabatic sense.

Computational studies were performed for pulsed operation of argon ICPs. The peak electron temperature at the leading edge of the power-on pulse increased with decreasing duty cycle as the same power was deposited into a smaller inventory of electrons at the end of the longer afterglow. As the PRF decreased, the peak in electron temperature at the leading edge of the power-on pulse increased and the ionization source was more confined beneath the coil. The spatial dynamics of plasma potential and electron temperature did not vary significantly with peak power. As the pressure decreased, the diffusion rates increased, resulting in a more diffused electron density profile. The electron density was observed to peak off axis during the power-on phase due to a larger ionization source beneath the coils. The peak in the electron density then moved to the center of the reactor during the late active glow as the electron density profile became more diffusion dominated. The model captured the dynamics in electron density observed in experiments.

ACKNOWLEDGMENTS

This work is supported by the National Science Foundation (Grant No. CTS99-74962), the Semiconductor Research Corp, DARPA/AFOSR, and Applied Materials.

[1]W. Z. Collison, T. Q. Ni, and M. S. Barnes, J. Vac. Sci. Technol. A **16**, 100 (1998).
[2]J. Y. Choe, I. P. Herman, and V. M. Donnelly, J. Vac. Sci. Technol. A **15**, 3024 (1997).
[3]R. W. Boswell and R. K. Porteous, J. Appl. Phys. **62**, 3123 (1987).
[4]S. Samukawa and T. Meino, Plasma Sources Sci. Technol. **5**, 132 (1996).
[5]S. Samukawa, Appl. Phys. Lett. **68**, 316 (1996).
[6]S. Samukawa, K. Noguchi, J. I. Colonell, K. H. A. Bogart, M. V. Malyshev, and V. M. Donnelly, J. Vac. Sci. Technol. B **18**, 834 (2000).

[7]G. A. Hebner and C. B. Fleddermann, J. Appl. Phys. **82**, 2814 (1997).
[8]S. Ashida, M. R. Shim, and M. A. Leiberman, J. Vac. Sci. Technol. A **14**, 391 (1996).
[9]T. Ishigaki, X. Fan, T. Sakuta, T. Banjo, and Y. Shibuya, Appl. Phys. Lett. **71**, 3787 (1997).
[10]M. V. Malyshev, V. M. Donnelly, S. Samukawa, and J. I. Colonell, J. Appl. Phys. **86**, 4813 (1999).
[11]M. V. Malyshev and V. M. Donnelly, Plasma Sources Sci. Technol. **9**, 353 (2000).
[12]M. Meyyappan, J. Vac. Sci. Technol. A **14**, 2122 (1996).
[13]S. Ashida, C. Lee, and M. A. Leiberman, J. Vac. Sci. Technol. A **13**, 2498 (1995).
[14]M. A. Leibermann and S. Ashida, Plasma Sources Sci. Technol. **5**, 145 (1996).
[15]S. Ashida and M. A. Leibermann, Jpn. J. Appl. Phys., Part 1 **36**, 854 (1997).
[16]D. P. Lymberopoulos, V. I. Kolobov, and D. J. Economou, J. Vac. Sci. Technol. A **16**, 564 (1998).
[17]V. Midha and D. J. Economou, Plasma Sources Sci. Technol. **9**, 256 (2000).
[18]B. Ramamurthi and D. J. Economou, Bull. Am. Phy. Soc. **45**, 40 (2000).
[19]P. A. Miller, G. A. Hebner, K. E. Greenberg, and P. D. Pochan, J. Res. Natl. Inst. Stand. Technol. **100**, 427 (1995).
[20]P. Subramonium and M. J. Kushner, J. Vac. Sci. Technol. A **20**, 325 (2002).
[21]R. L. Kinder and M. J. Kushner, J. Vac. Sci. Technol. A **19**, 76 (2001).
[22]W. Z. Collison and M. J. Kushner, Appl. Phys. Lett. **68**, 903 (1996).
[23]Kuck and Associates, Inc. http://www.kai.com/parallel/kappro/
[24]D. L. Scharfetter and H. K. Gummel, IEEE Trans. Electron Devices **16**, 64 (1969).
[25]S. Rauf and M. J. Kushner, J. Appl. Phys. **82**, 2805 (1997).
[26]K. Tachibana, Phys. Rev. A **34**, 1007 (1986).
[27]D. Rapp and P. Englander-Golden, J. Chem. Phys. **43**, 1464 (1965).
[28]R. H. McFarland and J. D. Kinney, Phys. Rev. **137**, 1058 (1965).
[29]I. P. Zapesochnyi and L. L. Shimon, Opt. Spectrosc. **11**, 155 (1966).
[30]L. Virens, Phys. Lett. **8**, 260 (1964).